

Fluorinated Poly(aryl piperidinium) Membranes for Anion Exchange Membrane Fuel Cells

Xingyu Wu, Nanjun Chen, Chuan Hu, Harm-Anton Klok, Young Moo Lee,* and Xile Hu*

Anion-exchange-membrane fuel cells (AEMFCs) are a cost-effective alternative to proton-exchange-membrane fuel cells (PEMFCs). The development of high-performance and durable AEMFCs requires highly conductive and robust anion-exchange membranes (AEMs). However, AEMs generally exhibit a trade-off between conductivity and dimensional stability. Here, a fluorination strategy to create a phase-separated morphological structure in poly(aryl piperidinium) AEMs is reported. The highly hydrophobic perfluoroalkyl side chains augment phase separation to construct interconnected hydrophilic channels for anion transport. As a result, these fluorinated PAP (FPAP) AEMs simultaneously possess high conductivity ($>150 \text{ mS cm}^{-1}$ at 80°C) and high dimensional stability (swelling ratio $<20\%$ at 80°C), excellent mechanical properties (tensile strength $>80 \text{ MPa}$ and elongation at break $>40\%$) and chemical stability ($>2000 \text{ h}$ in 3 M KOH at 80°C). AEMFCs with a non-precious Co–Mn spinel cathode using the present FPAP AEMs achieve an outstanding peak power density of 1.31 W cm^{-2} . The AEMs remain stable over 500 h of fuel cell operation at a constant current density of 0.2 A cm^{-2} .

especially in long-range and heavy-duty applications.^[1] One limitation of PEMFCs is their high cost due to their reliance on expensive materials.^[2] By switching from an acidic to an alkaline environment, anion-exchange-membrane fuel cells (AEMFCs) are a cost-effective alternative to PEMFCs.^[3] The development of high performance and durable AEMFCs requires robust anion exchange membranes (AEMs) with excellent chemical stability, high ion conductivity, and dimensional stability.^[4]

AEMs consist of a polymer backbone, immobilized cationic groups, and free anions (typically OH^-) that balance the charges of the cationic groups. Two main challenges in developing desirable membranes for AEMFCs are the chemical stability and the trade-off between ion conductivity and dimensional stability.^[5] To address the challenge of chemical stability, the polymer backbones and cationic

groups need to be rationally designed.^[6] Recently, poly(aryl piperidinium)s (PAPs) have been demonstrated to have excellent chemical stability.^[7] Specifically, the alkaline stability of piperidinium (DMP) cation is 21 times higher than that of benchmark benzyl trimethylammonium (BTMA) under alkaline conditions.^[8] The improved stability of the former is due to the low ring strain and conformational constraints imposed by the ring structure that significantly increase the transition state energy of the nucleophilic substitution and elimination degradation reactions.^[8] PAP-based AEMs in combination with durable DMP with aryl-ether free polyaromatic backbones were stable in 2 M KOH at 120°C over 336 h .^[7b]

The second challenge, namely, the trade-off between ion conductivity and dimensional stability, remain problematic for most AEMs including those based on PAPs. These membranes typically require a high concentration of OH^- charge carriers (e.g., with an ion exchange capacity (IEC) of $2\text{--}3 \text{ meq. g}^{-1}$) to achieve conductivity of about 150 mS cm^{-1} at 80°C , which is the benchmark conductivity for proton conducting membranes such as Nafion.^[9] However, high IECs usually lead to high water uptake and swelling ratio, which in turn causes poor dimensional stability. For instance, Olsson et al.^[7b] reported a poly(p-terphenyl *N,N*-dimethyl piperidinium) (PTPipQ1) membrane (IEC, 2.8 meq. g^{-1}) with high water uptake ($>145\%$ at 20°C). Various strategies, such as copolymerization,^[10] side-chain grafting,^[7b,11] branching,^[12] and crosslinking,^[13] have been applied to ameliorate the dimensional stability of PAP AEMs.


1. Introduction

The past few years have witnessed growing interests in deploying proton-exchange-membrane fuel cells (PEMFCs) vehicles,

X. Wu, N. Chen, X. Hu
Laboratory of Inorganic Synthesis and Catalysis (LSCI)
Institute of Chemical Sciences and Engineering (ISIC)
École Polytechnique Fédérale de Lausanne (EPFL)
Lausanne 1015, Switzerland
E-mail: xile.hu@epfl.ch

C. Hu, Y. M. Lee
Department of Energy Engineering
College of Engineering
Hanyang University
Seoul 04763, South Korea
E-mail: ymlee@hanyang.ac.kr

H.-A. Klok
Laboratoire des Polymères
Institut des Matériaux and Institut des Sciences et Ingénierie Chimiques
École Polytechnique Fédérale de Lausanne (EPFL)
Lausanne 1015, Switzerland

 The ORCID identification number(s) for the author(s) of this article can be found under <https://doi.org/10.1002/adma.202210432>

© 2023 The Authors. Advanced Materials published by Wiley-VCH GmbH. This is an open access article under the terms of the Creative Commons Attribution License, which permits use, distribution and reproduction in any medium, provided the original work is properly cited.

DOI: 10.1002/adma.202210432

Despite these efforts, PAP AEMs still rarely have both high conductivity and high dimensional stability.

We hypothesized that morphology control can overcome the trade-off between ion conductivity and dimensional stability for AEMs.^[14] This hypothesis was inspired by Nafion membranes, which have both high ion conductivity and high dimensional stability.^[15] Nafion membranes consist of a highly hydrophobic perfluorocarbon backbone and hydrophilic sulfonic ion groups. The substantial hydrophobic/hydrophilic difference in the polymer leads to a good microphase separation. Recently, some fluorene-based AEMs with obvious hydrophobic/hydrophilic microphase separation were reported.^[16] However, it is difficult to achieve microphase separation for PAP AEMs because the hydrocarbon backbone of PAP has only modest hydrophobicity, and the hydrophobic/hydrophilic difference between different regions of PAP AEMs is not high due to the short distance of the hydrophilic piperidinium cations to the hydrophobic backbones.^[17] Here, we report a fluorination strategy to enhance microphase separation in PAP AEMs. By incorporating highly hydrophobic perfluoroalkyl side chains to the PAP polymer backbones, we created FPAP AEMs with interconnected hydrophilic channels inside the hydrophobic polymers. Such a morphology facilitates OH⁻ transport while maintaining a low swelling ratio, leading to AEMs with both high conductivity and high dimensional stability.

2. Results and Discussion

2.1. Synthesis and Characterization

Fluorene is a widely used aromatic compound, consisting of two benzene rings fused on either side of cyclopentane. This structural feature makes it feasible to introduce various functional moieties at the 9-position of fluorene.^[18] Initial attempts to introduce perfluoroalkyl moieties on fluorene in the presence of perfluoro-1-iodohexane yielded 9,9'-spirobi[fluorene] as the main product. To avoid this undesired reaction, we decided to add alkyl spacers between the fluorene and the perfluoroalkyl moieties. Therefore, semi-perfluoroalkyl halides [I-(CH₂)₂(CF₂)_xCF₃] with an -(CH₂)₂- spacer were reacted with fluorene to give semi-fluoroalkyl fluorenes (Figure 1a). A series of semi-fluoroalkyl fluorene monomers with different -CF₂- length (*n* = 1, 5, 9) were synthesized and their chemical structures were confirmed by nuclear magnetic resonance (NMR) (Figures S1, S2, and S3, Supporting Information). The fluorinated poly(aryl piperidone)s were synthesized via a trifluoromethanesulfonic acid (TfSA) catalyzed polymerization of p-terphenyl (TP), a semi-fluoroalkyl fluorene monomer, and N-methyl-4-piperidone. Then, the fluorinated poly(aryl piperidinium)s (FPAP-*x*, where *x* refers to the mass percentage of fluorine element) were synthesized via a Menshutkin reaction between fluorinated poly(aryl piperidone)s and iodomethane (Figure 1b). Intrinsic viscosity is widely used as the indicator of molecular weight of poly(aryl piperidinium)s.^[7a,10a] FPAP-3 and FPAP-7 exhibited much higher viscosity than the pristine poly(aryl piperidinium) (PAP) (2.8 dL g⁻¹, Table 1), the PAP-TP-85 polymer (4.71 dL g⁻¹) reported by Wang et al.^[7a] and the PFTP-13 polymer (4.08 dL g⁻¹) reported by Chen et al.,^[10a] suggesting a higher molecular weights of FPAPs compared to these other polymers. The viscosity of FPAP-11 (4.5 dL g⁻¹) is substantially

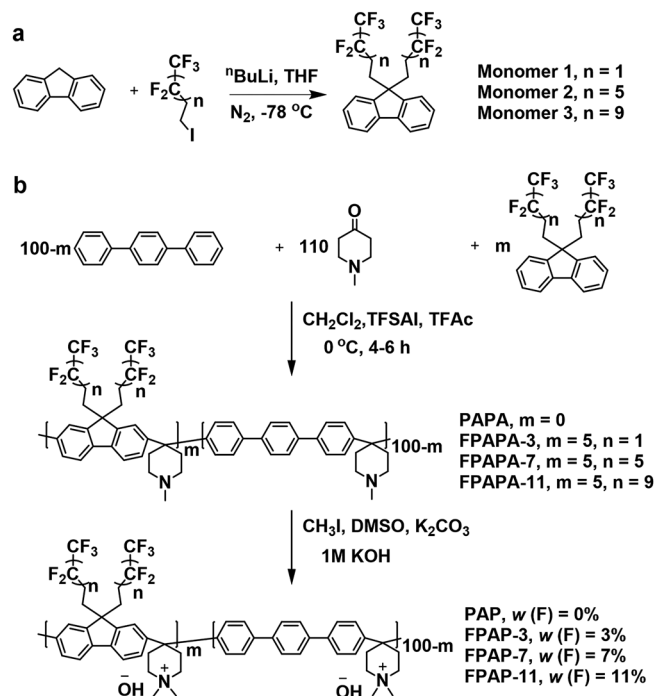


Figure 1. a,b) Synthesis of semi-perfluoroalkyl fluorene monomers (a) and fluorinated poly(aryl piperidinium)s (b).

lower than that of FPAP-3 (6.5 dL g⁻¹). We speculated that the higher molecular weight of monomer 3 (1258.5 g mol⁻¹) compared to monomer 1 (458.5 g mol⁻¹) led to a lower mobility of molecules, which decreased the degree of polymerization.

The chemical structures of FPAP-*x* were confirmed by NMR spectroscopy. In the ¹H NMR spectrum of FPAP-3, two peaks at 2.7 ppm and 1.2 ppm were assigned to the alkyl spacer of the semi-perfluoroalkyl fluorene monomer 1 (Figures S4 and S5, Supporting Information). In its ¹⁹F NMR spectrum, two peaks at -117 ppm and -84.5 ppm were attributed to the perfluoroalkyl moieties of monomer 1 (Figures S5 and S6, Supporting Information). Likewise, the chemical structures of FPAP-7 and FPAP-11 polymers were confirmed by ¹H and ¹⁹F NMR (Figures S7 and S8, Supporting Information). The weight percentage of fluorine element was determined (by NMR) as 3%, 7.4%, and 10.7% for FPAP-3, FPAP-7, and FPAP-11, respectively (Table 1).

2.2. Mechanical Property and Morphology

The present FPAP polymers are highly processable and can be easily cast into thin membranes with a size over 500 cm² and a thickness ≈20 μm (Figure 2a). The FPAP AEMs were flexible and remained intact after several cycles of stretching, twisting, kneading, and recovering (Video S1, Supporting Information). The tensile strength and elongation at break of FPAP AEMs are enhanced compared to those of pristine PAP membrane and commercial FAA-3-50 membrane^[12a] (Figure 2f). Increasing the fluorine percentage from 3 to 11% leads to decreased tensile strength and elongation at break due to a decrease of molecular weight (Table 1).^[7a,16a-b] The FPAP-3 membrane exhibits much higher tensile strength (84 MPa) and elongation at break (40%)

Table 1. IEC, fluorine percentage, intrinsic viscosity (η), water uptake (WU), swelling ratio (SR), and conductivity (σ) of PAP and FPAP-x AEMs.

AEMs	IEC [meq. g ⁻¹]			Fluorine percentage [%]	η [dL g ⁻¹]	WU [%]		SR [%]		σ [mS cm ⁻¹]	
	Theor.	NMR	Titra.			40 °C	80 °C	40 °C	80 °C	40 °C	80 °C
PAP	2.80	2.81	2.84	0	2.8	94	109	30.7	33.2	81	138
FPAP-3	2.71	2.70	2.73	3.0	6.5	85	97	13.7	15.5	97	148
FPAP-7	2.57	2.54	2.55	7.4	5.5	77	82	11.5	13.1	108	166
FPAP-11	2.45	2.42	2.47	10.7	4.5	67	72	8.6	9.6	102	158

than the pristine PAP membrane (52 MPa tensile strength and 24% elongation at break). Similarly, FPAP AEMs display higher storage modulus at high temperature compared to the pristine PAP AEMs due to higher molecular weight and the entanglement of perfluoroalkyl chains, as revealed from dynamic mechanical analysis (DMA) (Figure 2g; Figure S10, Supporting Information). The FPAP-3 AEM displays excellent thermomechanical properties, and its storage modulus reaches 1900 MPa at 80 °C.

The morphologies of the FPAP AEMs were probed by atomic force microscopy (AFM) (Figure 2b–e; Figure S11, Supporting Information). The blue region indicates the aggregation of the hydrophilic piperidinium segment, while the grey region indicates

the aggregation of the hydrophobic aryl and perfluoroalkyl segment. The FPAP AEMs exhibited clear hydrophobic/hydrophilic microphase separation with consecutive ion channels. The microphase separation of FPAPs is increased with an increase of fluorine percentages because the introduction of highly hydrophobic perfluoroalkyl moieties increases the difference between the hydrophobic and hydrophilic segments. The hydrophobicity of FPAP AEMs was confirmed by the water drop contact angle tests, which indicated that the water contact angle increased from 69° to 99° when the fluorine percentage increases from 3% to 11% (Figure S9 (Supporting Information) and inserted images in Figure 2b–e). Meanwhile the hydrophilic regions are

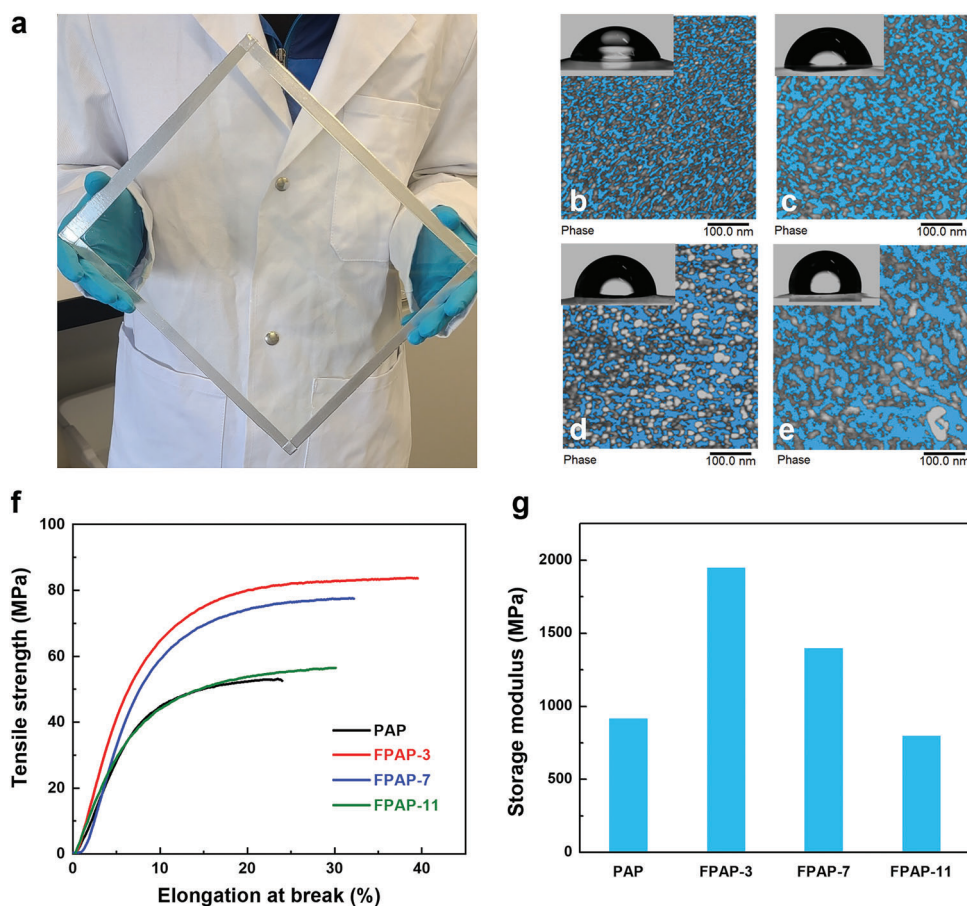


Figure 2. a) Photograph of a transparent FPAP-3 AEM with a thickness of $\approx 20 \mu\text{m}$. b–e) Atomic force microscopy images of PAP (b), FPAP-3 (c), FPAP-7 (d), and FPAP-11 (e) AEMs with inset pictures of water drop contact angle tests. f) Mechanical properties of FPAP AEMs. g) Storage modulus of the FPAP-3 membrane.

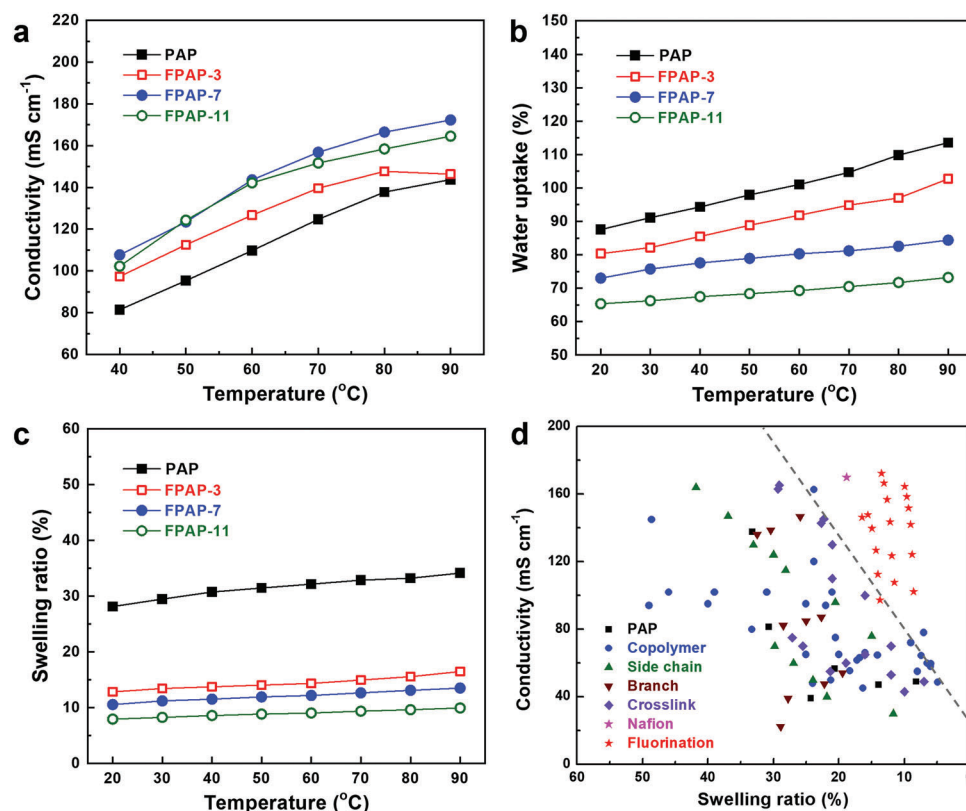


Figure 3. a) OH^- conductivity of FPAP AEMs at different temperatures and 100% RH. b) Water uptake and c) swelling ratio of FPAP AEMs. d) OH^- conductivity versus swelling ratio (Nafion NR-211,^[9] typical PAP AEMs,^[7b,19] copolymerization,^[10] side chain grafting,^[7b,11] branching,^[12] crosslinking^[13] PAP AEMs as reported).

interconnected into ion-transporting channels, thus achieving high OH^- conductivity and water vapor permeability (Table 1; Table S1, Supporting Information).

2.3. Conductivity and Dimensional Stability

The FPAP AEMs exhibit a high OH^- conductivity at 40 °C (90–110 mS cm^{-1} , Figure 3a) with IEC of 2.4 to 2.7 meq. g^{-1} . The conductivity increases with temperature. Fluorination improves significantly both the conductivity and dimensional stability of PAP AEMs. For example, FPAP-3 membrane has a conductivity of 97 mS cm^{-1} and a swelling ratio of 13.7% at 40 °C. Both the conductivity and dimensional stability improve with increasing fluorine percentage (Figure 3a–c), except that FPAP-11 has a slightly lower conductivity than FPAP-7. By comparison PAP membrane has a conductivity of only 81 mS cm^{-1} despite having a higher IEC and a swelling ratio of 30.7% at 40 °C. The increase of conductivity upon fluorination may be attributed to an improved hydrophobic–hydrophilic microphase separation (Figure 2b–e). Shen et al.^[8c] demonstrated that piperidinium-side-chain terminated AEMs with distinct microphase separation had improved ion conductivity. Chen et al.^[10b] reported that the ion conductivity of PDTP- x AEMs increased with the size of hydrophilic channels. Li et al.^[16a] showed that the connectivity of hydrophilic domains in PFBA-QA-b membrane is important for ion and water transport. In the present work, the perfluoroalkyl segments

induce the formation of large hydrophilic domains in the polymer chains, yielding interconnected ion transport channels. This continuous phase microstructure results in high OH^- conductivity. In these FPAP membranes, the hydrophilic domains are surrounded by rigid hydrophobic domains (terphenyl and fluorene segments), which restrict the hydrophilic domains from absorbing a large amount of water, thereby decreasing the water swelling ratio. Overall, FPAP AEMs exhibit similar conductivity and swelling ratios to those of Nafion membranes^[9] (Figure 3d; Table S3, Supporting Information).

2.4. Alkaline and Oxidation Stabilities

The potential degradation sites of FPAP AEMs are the fluorene segments, more specifically, the spacers between perfluoroalkyl and aryl moieties, which could undergo elimination reaction under alkaline conditions at high temperature (Figure 4a). To probe the possible degradation reaction by ^{19}F NMR, we used a model PFAP membrane made of polymer with 20% fluorinated fluorene monomer. An elimination reaction was observed in 3 M KOH at 80 °C. In the ^1H NMR spectra of the reaction mixture, a new peak at $\delta = 5.2$ ppm appeared, which was assigned to the hydrogens of a $\text{C}=\text{C}$ bond (a', Figure 4c). Based on this result, the elimination was assigned to HF elimination in the semifluorinated side chain (Figure 4a). After 100 h, the elimination reached its saturation and $\approx 50\%$ of the side chain had undergone the

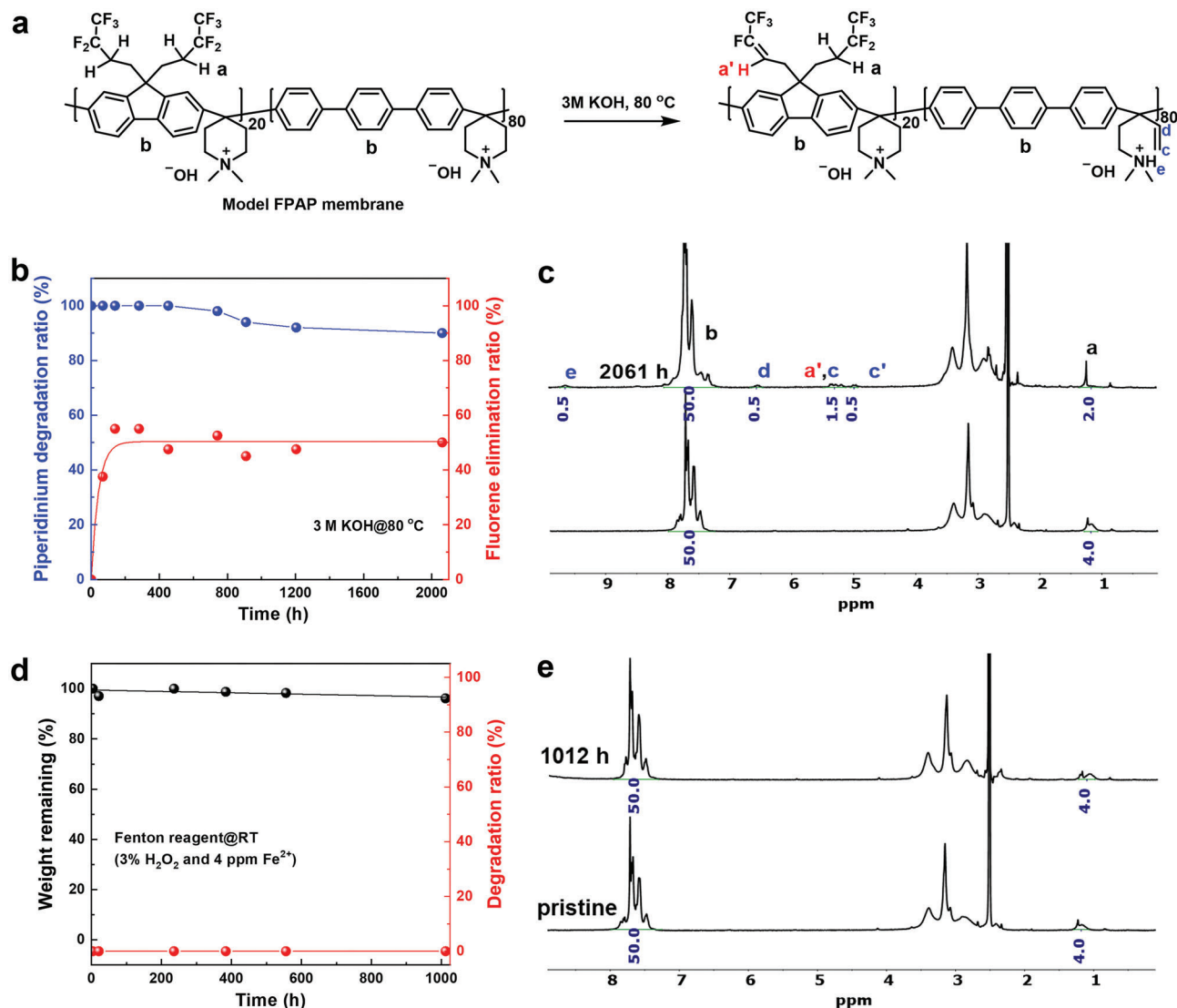


Figure 4. Alkaline stability of model FPAP membrane in 3 M KOH at 80 °C. a) Degradation mechanism and b) piperidinium remaining ratio and fluorene elimination ratio at different interval time. c) ¹H NMR spectra before and after 2061 h immersion. Oxidation stability of model FPAP membrane in Fenton solution (3 wt% H₂O₂ and 4 ppm Fe²⁺) at room temperature. d) Weight remaining and degradation ratio at different interval time. e) ¹H NMR spectra before and after 1012 h immersion.

elimination (Figure 4b). Increasing the immersion time to 2000 h in 3 M KOH at 80 °C did not lead to further elimination (Table S2 and Figure S12, Supporting Information). Notably, this elimination does not remove the fluorinated alkyl side chain from the polymer backbones. As for the piperidinium groups, degradation was visible only after 741 h; and only ≈10% of piperidinium groups were degraded after 2061 h. These results indicate excellent alkaline stability of FPAP AEMs (Figure 4b; Table S2, Supporting Information).

Recently, the formation of HO and HO₂ radicals on the electrodes and inside the membrane during the operation of AEM-FCs was reported to severely degrade AEMs.^[4b,20] Thus it is necessary to probe the oxidation stability of AEMs.^[21] For this purpose, a Fenton reagent (3 wt% H₂O₂ and 4 ppm Fe²⁺) was widely used to simulate the practical operation environment of fuel cells.^[22] We immersed the model PFAP membrane in a solution

of Fenton reagent at room temperature and 80 °C. As shown in Figure 4d,e and Figures S13–S15 (Supporting Information), no weight loss and molecular structure change were observed, indicating the excellent oxidation stability of FPAP AEMs. Note that although the model PFAP membrane is useful for stability study, due to the very high F content, the corresponding polymer has a low intrinsic viscosity and the membrane is brittle.^[10a] As such, the model PFAP membrane was not further studied.

2.5. Fuel Cell Performance and Durability

The FPAP-3 membrane with a thickness of ≈20 μm was used to fabricate membrane electrode assemblies (MEAs) via two methods, namely, catalyst-coated membrane (CCM) and catalyst-coated substrate (CCS). The peak power densities (PPDs) of

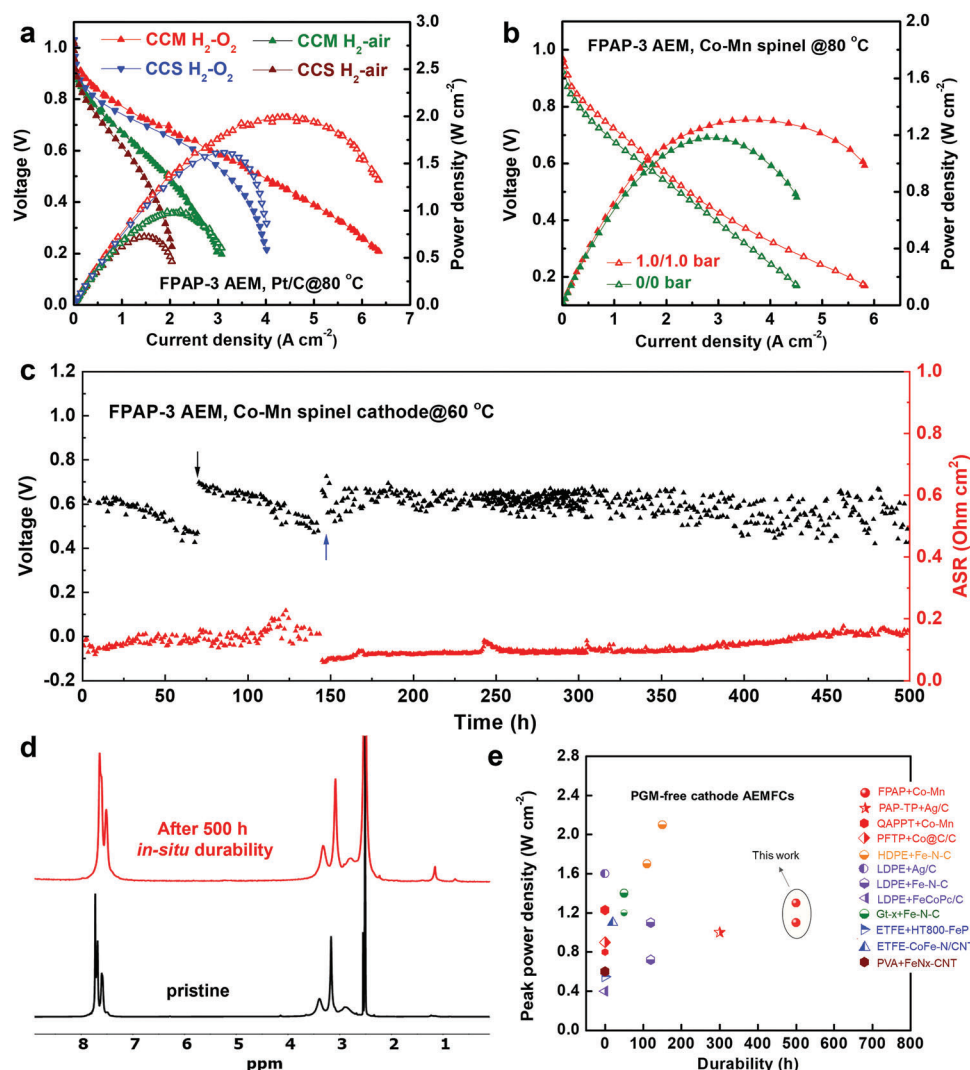


Figure 5. a, b) AEMFC performance based on a FPAP-3 membrane with Pt/C (a) and Co–Mn spinel (b) cathode catalysts. c) AEMFC durability test under a constant current density of 0.2 A cm^{-2} at $60 \text{ }^\circ\text{C}$. d) ^1H NMR spectra of FPAP-3 membrane before and after AEMFC durability test for 500 h. e) Comparison of the peak power density and durability for state-of-the-art AEMFCs with PGM-free cathodes.^[3d,e,7a,10a,23]

PGM-based AEMFCs prepared from CCM method were as high as 2 W cm^{-2} at $80 \text{ }^\circ\text{C}$ in $\text{H}_2\text{-O}_2$, while those of AEMFCs prepared from CCS method were as high as 1.6 W cm^{-2} (Figure 5a). Thus, the CCM method gave a better interface contact between catalysts and the membrane.^[24] The PPDs of PGM-based AEMFCs prepared from CCM and CCS methods reached 1 W cm^{-2} and 0.75 W cm^{-2} in $\text{H}_2\text{-air}$ (CO_2 free), respectively. Analogous AEMFCs with FPAP-7 or FPAP-11 as the AEM have slightly lower PPDs (Figure S16, Supporting Information).

One of the key advantages of AEMFCs over PEMFCs is the possibility to use PGM-free catalysts, especially for the oxygen reduction reaction (ORR). Thus, a typical PGM-free ORR cathode catalyst, Co–Mn spinel, was synthesized^[3e] and assembled with a FPAP-3 membrane via the CCS method for AEMFC test. AEMFCs with a Co–Mn spinel cathode reached 1.1 W cm^{-2} without backpressure and 1.3 W cm^{-2} with 1.0/1.0 A/C backpressure at $80 \text{ }^\circ\text{C}$ in $\text{H}_2\text{-O}_2$, respectively (Figure 5b). Although comparison of reported AEMFCs is not straightforward because of different cat-

alysts, cell configuration and operation conditions, our present AEMFCs with a FPAP-3 membrane and a Co–Mn spinel cathode achieves one of the topmost PPDs among AEMFCs with PGM-free cathodes (Figure 5e; Table S4, Supporting Information).

Figure 5c showed the durability test of AEMFCs based on FPAP-3 membrane and Co–Mn spinel cathode with a constant current density of 0.2 A cm^{-2} at $60 \text{ }^\circ\text{C}$. The transient fluctuation of cell voltage indicated the continuous formation and removal of water droplet during test. The cell was first operated at a constant current density of 0.4 A cm^{-2} . The voltage decreased from 0.6 to 0.5 V and area surface resistance (ASR) increased from 0.15 to $0.2 \text{ } \Omega \text{ cm}^2$ after 70 h. Then the current density was adjusted to 0.2 A cm^{-2} (black arrow) and the cell voltage jumped up to 0.7 V but again decreased to 0.5 V after 80 h. To identify the origin of voltage loss, the catalytic layers were removed and replaced with fresh catalysts for further durability test at 0.2 A cm^{-2} . The voltage of refreshed cell (blue arrow) recovered and remained stable at 0.6 V, suggesting that the voltage loss was likely due to the

degradation of the catalytic layers. From then on, an AEMFC with a FPAP-3 membrane and a Co–Mn spinel cathode catalyst could operate stably over 350 h at 0.6 V and 0.2 A cm⁻². Importantly, the FPAP-3 membrane was not damaged after the above 500 h durability test as no chemical structure degradation was detected by NMR (Figure 5d). To the best of our knowledge, this is the first reported AEMFC with a PGM-free cathode that exhibits durability over 350 h (Figure 5e). Most AEMFCs based on PGM-free cathodes showed durability of less than 100 h.^[3e,10a,23] Adabi et al.^[3d] reported that AEMFCs with HDPE-based AEMs and a Fe–N–C cathode had a durability of 150 h. Wang et al.^[7a] reported that AEMFCs with PAP-based AEMs and an Ag-based cathode had a durability of 300 h.

3. Conclusion

We have developed a fluorination strategy to achieve improved microphase separation and construct interconnected hydrophilic channels for PAP AEMs. The resulting FPAP AEMs exhibit both high OH⁻ conductivity (>150 mS cm⁻¹ at 80 °C) and high dimensional stability (swelling ratio < 20% at 80 °C), which had been elusive for this class of promising AEMs. In addition, the FPAP AEMs have excellent mechanical properties (tensile strength > 80 MPa and elongation at break > 40%) and chemical stability (>2000 h in 3 M KOH at 80 °C). AEMFCs based on these FPAP AEMs achieve peak power densities comparable to state of the art AEMFCs. In particular, the AEMFCs with a PGM-free (Co–Mn spinel) cathode achieved a high PPD of 1.3 W cm⁻² at 80 °C. Operational stability of over 500 h of the FPAP membranes has been demonstrated.

4. Experimental Section

Materials: Para-terphenyl (TP), N-methyl-4-piperidone, iodomethane, potassium carbonate (K₂CO₃), ⁿBuLi (2.5 M solution in hexane) and dimethyl sulfoxide (DMSO) were purchased from Sigma-Aldrich. Trifluoromethanesulfonic acid (TFSA), 1,1,1,2,2-pentafluoro-4-iodobutane, 1,1,1,2,2,3,3,4,4,5,5,6,6-tridecafluoro-8-iodooctane and 2-(perfluorodecyl)ethyl iodide were purchased from Fluorochem. Fluorene and trifluoroacetic acid (TFA) were purchased from TCI. Dichloromethane (CH₂Cl₂), tetrahydrofuran (THF), and ethyl acetate were purchased from Thermo Fisher Scientific Incorporation. All chemicals were used directly without further purification.

Synthesis of Semi-Perfluoroalkyl Fluorene Monomers: A typical synthetic procedure of semi-perfluoroalkyl fluorene monomers is described as follows.^[25] To a solution of fluorene (1.50 g, 9 mmol) in anhydrous THF (20 mL) equipped with a magnetic stirrer, ⁿBuLi (2.5 M solution in hexane, 4 mL, 10 mmol) was added dropwise at –78 °C under an N₂ atmosphere. The solution was then warmed to 0 °C and was stirred for 5 min. After being cooled back to –78 °C, a solution of 1,1,1,2,2-pentafluoro-4-iodobutane (2.74 g, 10 mmol) in THF (5 mL) was added dropwise to the mixture. The solution was warmed to room temperature and was stirred for 1 h. After being cooled back to –78 °C, another portion of ⁿBuLi (2.5 M solution in hexane, 4 mL, 10 mmol) was added dropwise under an N₂ atmosphere. The solution was again warmed to 0 °C and was stirred for 5 min. After being cooled back to –78 °C, another portion of 1,1,1,2,2-pentafluoro-4-iodobutane (2.74 g, 10 mmol) in THF (5 mL) was added dropwise to the mixture. The final solution was warmed to room temperature, stirred for 1 h, quenched with excess water (150 mL), and extracted with hexane for three times. The organic layer was washed with brine water, dried with anhydrous MgSO₄, concentrated with rotavapor, purified through a short column of silica gel with hexane as the eluent. The crude product was crystallized from CH₂Cl₂ to give a

colorless crystal of semi-perfluoroalkyl fluorene monomer 1 (3.5 g 86%). Semi-perfluoroalkyl fluorene monomers 2 and 3 was synthesized by replacing 1,1,1,2,2-pentafluoro-4-iodobutane with 1,1,1,2,2,3,3,4,4,5,5,6,6-tridecafluoro-8-iodooctane and 2-(perfluorodecyl)ethyl iodide, respectively.

Synthesis of Fluorinated Poly(aryl piperidine) (FPAPA-x): A typical synthetic procedure of fluorinated poly(aryl piperidine) (FPAPA-x) is described as below. To a flask equipped with an overhead mechanical agitator, TP (0.95 eq.), fluorene monomer 1 (0.05 eq.) and N-methyl-4-piperidone (1.1 eq.) were added into CH₂Cl₂. After being stirred for 30 min at 0 °C, TFA and TFSA were added slowly to the solution in sequence. Upon the addition, the mixture's color changed to red and then purple. After being stirred for 4–6 h at 0 °C, the solution became very viscous and was then quenched by being poured into an excess amount of water. The white precipitate was cracked into small pieces, followed by washing three times with water, and finally being dried at 80 °C under vacuum for 24 h. The product was named as FPAPA-3, where 3 refer to the percentage of fluorine element. FPAPA-7 and FPAPA-11 were synthesized by replacing fluorene monomer 1 with monomer 2 and 3, respectively.

Synthesis of Fluorinated Poly(aryl piperidinium) (FPAP-x): A typical synthetic procedure of fluorinated poly(aryl piperidinium) (FPAP-x) is described as below. To a flask equipped with a magnetic stirrer, FPAPA-2 (1 g) was dissolved in DMSO (20 mL). Then K₂CO₃ (0.39 g) and iodomethane (0.2 mL) were added. The solution was stirred for 24 h at room temperature in the dark. The resulting solution was poured into ethyl acetate to give a precipitate. The latter was washed three times with water and dried at 80 °C under vacuum for 24 h. The product was named as FPAP-3, where 3 refer to the percentage of fluorine element. FPAP-7 and FPAP-11 were synthesized by replacing FPAPA-3 with FPAPA-7 and FPAPA-11, respectively.

Synthesis of Model FPAP Polymer: To a flask equipped with an overhead mechanical agitator, TP (0.80 eq.), fluorene monomer 1 (0.20 eq.) and N-methyl-4-piperidone (1.1 eq.) were added into CH₂Cl₂. After being stirred for 30 min at 0 °C, TFA and TFSA were added slowly to the solution in sequence. Upon addition, the solution's color changed to red and then purple. After being stirred for 4–6 h at 0 °C, the solution became very viscous and was then quenched by being poured into excess amount of water. The white precipitate was cracked into small pieces, washed three times with water, dried at 80 °C under vacuum for 24 h. Then, the as-obtained polymer (1 g) was dissolved in DMSO (20 mL). K₂CO₃ (0.39 g) and iodomethane (0.2 mL) were added. The solution was stirred for 24 h at room temperature in dark. The resulting solution was poured into ethyl acetate to give a precipitate, which was filtered, washed three times with water, and dried at 80 °C under vacuum for 24 h.

Membrane Preparation: A typical membrane preparation procedure is described as below. To a flask equipped with a magnetic stirrer, FPAP-3 (1 g) was dissolved in DMSO (20 mL). The solution was filtered through a 1 μm poly(tetrafluoroethylene) (PTFE) filter, casted onto a clean glass Petri dish. Then, the solution was allowed to evaporate at 90 °C for 12 h, 120 °C for 12 h, and then dried at 120 °C under vacuum for 24 h. The obtained FPAP-3 membrane in I⁻ form was peeled off from the glass Petri dish. FPAP-3 membrane in OH⁻ form was obtained by ion-exchanging in a KOH solution. FPAP-7 and FPAP-11 membranes were prepared by replacing FPAP-3 polymer with FPAP-7 and FPAP-11 polymers, respectively.

Intrinsic Viscosity: The intrinsic viscosity ($[\eta]$) was measured by a Schott Viscometry System (AVS 370, Germany) equipped with an Ubbelohde viscometer (SI Analytics, Type 530 13: Capillary No. 1c, K = 0.03) and an automatic piston burette (TITRONIC universal) at 25 °C. The polymer was first dissolved into DMSO with five different concentrations (3.0, 2.5, 2.0, 1.5, 1.0 mg dL⁻¹). Then, the solution was filled into the Ubbelohde viscometer. The efflux time was measured four times for each concentration and the average value was adopted. The reduced viscosity (η_{red}) and inherent viscosity (η_{inh}) were calculated by:

$$\eta_{red} = \frac{t_s - t_b}{c} \quad (1)$$

$$\eta_{\text{inh}} = \frac{\ln\left(\frac{t_s}{t_b}\right)}{c} \quad (2)$$

where t_s (s) and t_b (s) are the efflux time of DMSO and the polymer solution, respectively, c (g dL⁻¹) is the concentration. η_{red} and η_{inh} were plotted versus c in linear and intrinsic viscosity ($[\eta]$) was averaged by $\eta_{\text{red},c=0}$ and $\eta_{\text{inh},c=0}$.

Nuclear Magnetic Resonance: ¹H, ¹³C, and ¹⁹F NMR spectra of monomers, protonated FPAPA-x and model FPAP polymers, as well as the FPAP-x, were measured by a Bruker Avance 400 spectrometer. The polymer was dissolved in DMSO-*d*₆ with 5% vol% TFA doping, which can shift water peaks to reveal piperidine/piperidinium peaks. The ion exchange capacity (IEC) and fluorine percentage of PAP and FPAP-x AEMs were calculated from the corresponding ¹H NMR spectra.

IEC Measurement: The IEC values of FPAP-x membranes were measured by Mohr titration. A membrane sample in Br⁻ form (≈100 mg) was dried and weighted (W_{Br^-}). Subsequently, the membrane was immersed in 20 mL of 0.1 M NaNO₃ at 80 °C for 6 h and the immersion was repeated three times. The solution was titrated with a 0.01 M AgNO₃ solution with K₂CrO₄ as indicator. The IEC (meq. g⁻¹) was calculated by:

$$\text{IEC} = \frac{V_{\text{AgNO}_3} \times 0.01}{W_{\text{Br}^-} - 0.629 \times V_{\text{AgNO}_3}} \times 1000 \quad (3)$$

where V_{AgNO_3} is the volume of consumed AgNO₃ solution.

Water Contact Angle: Hydrophilicity of FPAP-x AEMs in I⁻ form was tested with an easy Drop from Krüss. The image was frozen immediately once the water drop contact with sample and water contact angle was recorded. Each membrane sample was measured at least three times and the average value was adopted.

Morphology: Morphological structures of FPAP-x AEMs in I⁻ form were observed from a Multimode 8 atomic force microscopy (AFM) (Veeco, NY, USA) with a NanoScope V controller in tapping mode.

Mechanical Properties: Mechanical properties of PAP and FPAP-x AEMs were measured by Universal Testing Machine (UTM; AGS-500N), Shimadzu, Tokyo, Japan) under ambient conditions with a 1 mm min⁻¹ strain rate.

Dynamic Mechanical Analysis: The storage modulus and tanδ of PAP and FPAP-x AEMs in I⁻ form were measured by a dynamic thermomechanical analysis (DMA, Q800. TA instrument, DE, USA) system. Membrane samples were cut into a rectangle shape with size of 9 mm × 20 mm and then applied with a 0.01 N preload force and a 125% force track under N₂ atmosphere. The sample was ramped at a rate of 4 °C min⁻¹ until 450 °C.

Water Uptake and Swelling Ratio: Water uptake (WU) and swelling ratio (SR) of PAP and FPAP AEMs can be calculated by:

$$\text{WU} (\%) = \frac{W_{\text{wet}} - W_{\text{dry}}}{W_{\text{dry}}} \times 100\% \quad (4)$$

$$\text{SR} (\%) = \frac{L_{\text{wet}} - L_{\text{dry}}}{L_{\text{dry}}} \times 100\% \quad (5)$$

where W_{dry} and L_{dry} were the weight and length of samples after drying in an oven at 80 °C under vacuum, W_{wet} and L_{wet} were the weight and length of samples after immersing in degassed deionized water for 12 h at different temperatures under N₂.

Conductivity Measurement: Ion conductivity of PAP and FPAP AEMs in OH⁻ form was measured by Autolab PGSTAT302N equipped with Scribner 740 MTS. Samples were cut into 10 mm × 30 mm size and tested with the alternative current (AC) impedance on a four-electrode cell with platinum electrodes from 1 Hz to 0.1 MHz. The assembly and measurement processes were operated under N₂ atmosphere to avoid CO₂ contamination. Impedance measurements were carried at different temperature and

100% RH. The ion conductivity σ (mS cm⁻¹) of PAP and FPAP AEMs can be calculated by:

$$\sigma = \frac{L}{AR} \quad (6)$$

where L (cm) is the distance between working and counter electrode, A (cm²) is the cross-sectional area calculated by the thickness (cm) and width (cm) of the membrane samples, R (kΩ) is the Ohm impedance obtained from electrochemical impedance spectra.

H₂ and Water Vapor Permeability: H₂ and water vapor permeability of PAP, FPAP-x AEMs were measured by a gas permeability testing system equipped with gas chromatography (GC, 490 Micro GC, Agilent Technologies, USA) and two mass flowmeters (MFC, M3030V, Line Tech, Korea). The measurements were carried under different RHs with 2.2 bar unilateral backpressure at 60 °C. Gas permeability P (Barrer, 1 Barrer = 10⁻¹⁰ cm³ (STP) cm cm⁻² s⁻¹ cmHg⁻¹) can be calculated by:

$$P = \frac{VM_{\text{gas}}d}{P_{\text{feed}}RTA\rho} \frac{d_p}{d_t} \quad (7)$$

where V (cm³), M_{gas} (g mol⁻¹), d (μm), and P_{feed} (760 mmHg) are the volume of measurement cell, molecular weight of permeating gas, membrane thickness and the pressure of feed gas, and R (L mmHg K⁻¹ mol⁻¹), T (K), A (cm²), and ρ (g cm⁻³) are the gas constant, testing temperature, effective area of samples and the density of permeating gas, respectively. $\frac{d_p}{d_t}$ denotes the change rate of permeated gas pressure over time.

Alkaline and Oxidation Stability: Alkaline stability of model FPAP membrane was evaluated in 3 M KOH at 80 °C over 2000 h. Oxidation stabilities of the model FPAP membrane were tested using a Fenton reagent (3 wt% H₂O₂ and 4 ppm Fe²⁺) at room temperature and 80 °C, respectively. After certain immersion time, the samples were taken out, rinsed with degassed deionized water, and ion-exchanged with 1 M NaI into I⁻ form. The structural changes were monitored by ¹H NMR.

Fuel Cell Performance: Membrane electrode assemblies with ≈20 μm FPAP-3 membranes were prepared via catalyst-coated membrane (CCM) and catalyst-coated substrate (CCS) methods, respectively. The anode and cathode slurries were sprayed onto both sides of membrane for the CCM method and onto gas diffusion layers (GDLs) for the CCS method. The anode slurry consists of Pt–Ru/C (40 wt% Pt, 20 wt% Ru, Hispec, Alfa Aesar, USA), carbon (Vulcan XC-72), poly(fluorenyl-co-biphenyl piperidinium) ionomer solution (PFBP, 5 wt% in DMSO), and PTFE powder using water/isopropanol (1:10) as solvent. The PGM cathode slurry was made from Pt/C (40 wt% Pt, Hispec, Alfa Aesar, USA), carbon (Vulcan XC-72), PTFE, and PFBP ionomer solution in water/isopropanol (1:10). The PGM-free cathode consists of a homemade Co–Mn spinel,^[3a] PFBP ionomer solution, and PTFE in water and isopropanol (1:10). The metal loadings of Pt–Ru anode and Pt cathode were 0.7 mg cm⁻². The metal loading of Co–Mn cathode was 1.2 mg cm⁻². All the catalyst slurries were sonicated for 30 min at 0 °C before spraying. Then, the prepared CCM or the CCS was immersed into 1 M NaOH at room temperature overnight and washed by DI water three times before use. Subsequently, the MEA was assembled with two gaskets and two graphite bipolar plates into a single fuel cell fixture with a torque of 40 in-lb, and the cell was evaluated in a fuel cell system (Fuel Cell Technologies, USA) at 60 °C and 80 °C. The cell was activated at a constant voltage of 0.5 V until a stable current density was achieved. Subsequently, the polar curve was recorded.

The durability of AEMFCs with FPAP-3 membrane and Co–Mn spinel cathode was monitored under a constant current density of 0.2 A cm⁻² at 60 °C with a 700/300 mL min⁻¹ H₂/O₂ flow rates. The anode/cathode relative humidity (RH) was slightly adjusted during durability testing to avoid electrode flooding or drying out. After durability testing, the membrane was taken out, washed by DI water and ethanol, ion-exchanged to I⁻ form, and re-dissolved in *d*⁶-DMSO to detect the structural changes by ¹H NMR.

Supporting Information

Supporting Information is available from the Wiley Online Library or from the author.

Acknowledgements

X.W. and N.C. contributed equally to this work. This work is supported by the EPFL and by the National Research Foundation of Korea (NRF) funded by the Ministry of Science and ICT (NRF-2018M1A2A2061979) and by the Technology Innovation Program (20010955) through the Korea Evaluation Institute of Industrial Technology (KEIT) funded by the Ministry of Trade, Industry & Energy (MOTIE) of South Korea. X. Wu, N. Chen, and X. Hu are inventors of a European priority patent application on the fluorinated AEMs partially described here.

Open access funding provided by Ecole Polytechnique Federale de Lausanne.

Conflict of Interest

X.W., N.J.C., and X.H. are inventors of an European priority patent application on the fluorinated AEMs partially described here.

Data Availability Statement

The data that support the findings of this study are available from the corresponding author upon reasonable request.

Keywords

anion-exchange membranes, anion-exchange-membrane fuel cells, fluorination, microphase separation, poly(aryl piperidinium)

Received: November 10, 2022

Revised: December 23, 2022

Published online:

- [1] a) D. A. Cullen, K. C. Neyerlin, R. K. Ahluwalia, R. Mukundan, K. L. More, R. L. Borup, A. Z. Weber, D. J. Myers, A. Kusoglu, *Nat. Energy* **2021**, *6*, 462; b) B. James, https://www.energy.gov/sites/prod/files/2018/04/f51/fcto_webinarslides_2018_costs_pem_fc_autos_trucks_042518.pdf (accessed: April 2018).
- [2] a) B. P. Setzler, Z. Zhuang, J. A. Wittkopf, Y. Yan, *Nat Nanotechnol* **2016**, *11*, 1020; b) B. D. James, J. M. Huya-Kouadio, C. Houchins, D. A. DeSantis, <https://www.energy.gov/sites/prod/files/2019/12/f70/fcto-sa-2018-transportation-fuel-cell-cost-analysis.pdf> (accessed: December 2018).
- [3] a) W. Ni, T. Wang, F. Heroguel, A. Krammer, S. Lee, L. Yao, A. Schüler, J. S. Luterbacher, Y. Yan, X. Hu, *Nat. Mater.* **2022**, *21*, 804; b) Y. Gao, Y. Yang, R. Schimmenti, E. Murray, H. Peng, Y. Wang, C. Ge, W. Jiang, G. Wang, F. J. DiSalvo, *Proc. Natl. Acad. Sci. USA* **2022**, *119*, e2119883119; c) H. A. Firouzjaie, W. E. Mustain, *ACS Catal.* **2019**, *10*, 225; d) H. Adabi, A. Shakouri, N. Ul Hassan, J. R. Varcoe, B. Zulevi, A. Serov, J. R. Regalbutto, W. E. Mustain, *Nat. Energy* **2021**, *6*, 834; e) Y. Yang, H. Peng, Y. Xiong, Q. Li, J. Lu, L. Xiao, F. J. DiSalvo, L. Zhuang, H. D. Abruña, *ACS Energy Lett.* **2019**, *4*, 1251.
- [4] a) N. Chen, Y. M. Lee, *Prog. Polym. Sci.* **2021**, *113*, 101345; b) W. E. Mustain, M. Chatenet, M. Page, Y. S. Kim, *Energy Environ. Sci.* **2020**, *13*, 2805.
- [5] a) G. Merle, M. Wessling, K. Nijmeijer, *J. Membr. Sci.* **2011**, *377*, 1; b) Y. Kim, Y. Wang, A. France-Lanord, Y. Wang, Y.-C. M. Wu, S. Lin, Y. Li, J. C. Grossman, T. M. Swager, *J. Am. Chem. Soc.* **2019**, *141*, 18152.
- [6] a) E. J. Park, Y. S. Kim, *J. Mater. Chem. A* **2018**, *6*, 15456; b) N. Chen, Y. Jin, H. Liu, C. Hu, B. Wu, S. Xu, H. Li, J. Fan, Y. M. Lee, *Angew. Chem., Int. Ed.* **2021**, *133*, 19421.
- [7] a) J. Wang, Y. Zhao, B. P. Setzler, S. Rojas-Carbonell, C. B. Yehuda, A. Amel, M. Page, L. Wang, K. Hu, L. Shi, *Nat. Energy* **2019**, *4*, 392; b) J. S. Olsson, T. H. Pham, P. Jannasch, *Adv. Funct. Mater.* **2018**, *28*, 1702758.
- [8] a) M. Marino, K. Kreuer, *ChemSusChem* **2015**, *8*, 513; b) T. H. Pham, J. S. Olsson, P. Jannasch, *J. Am. Chem. Soc.* **2017**, *139*, 2888; c) B. Shen, B. Sana, H. Pu, *J. Membr. Sci.* **2020**, *615*, 118537.
- [9] J. Peron, A. Mani, X. Zhao, D. Edwards, M. Adachi, T. Soboleva, Z. Shi, Z. Xie, T. Navessin, S. Holdcroft, *J. Membr. Sci.* **2010**, *356*, 44.
- [10] a) N. Chen, H. H. Wang, S. P. Kim, H. M. Kim, W. H. Lee, C. Hu, J. Y. Bae, E. S. Sim, Y.-C. Chung, J.-H. Jang, S.-J. Yoo, Y. Zhuang, Y. M. Lee, *Nat. Commun.* **2021**, *12*, 2367; b) N. Chen, C. Hu, H. H. Wang, S. P. Kim, H. M. Kim, W. H. Lee, J. Y. Bae, J. H. Park, Y. M. Lee, *Angew. Chem., Int. Ed.* **2021**, *133*, 7789.
- [11] a) F. H. Wang, Y. X. Li, C. H. Li, H. Zhu, *J. Membr. Sci.* **2021**, *620*, 118919; b) R. Ren, S. Zhang, H. A. Miller, F. Vizza, J. R. Varcoe, Q. He, *ACS Appl. Energy Mater.* **2019**, *2*, 4576.
- [12] a) X. Wu, N. Chen, H. A. Klok, Y. M. Lee, X. Hu, *Angew. Chem., Int. Ed.* **2022**, *61*, e202114892; b) L. Li, T. Jiang, S. Wang, S. Cheng, X. Li, H. Wei, Y. Ding, *ACS Appl. Energy Mater.* **2022**, *5*, 2462.
- [13] a) N. Chen, J. H. Park, C. Hu, H. H. Wang, H. M. Kim, N. Y. Kang, Y. M. Lee, *J. Mater. Chem. A* **2022**, *10*, 3678; b) X. M. Du, H. Y. Zhang, Y. J. Yuan, Z. Wang, *J. Power Sources* **2021**, *487*, 229429.
- [14] a) M. E. Tuckerman, D. Marx, M. Parrinello, *Nature* **2002**, *417*, 925; b) N. Li, M. D. Guiver, *Macromolecules* **2014**, *47*, 2175.
- [15] K. A. Mauritz, R. B. Moore, *Chem. Rev.* **2004**, *104*, 4535.
- [16] a) X. Li, K. Yang, Z. Wang, Y. Chen, Y. Li, J. Guo, J. Zheng, S. Li, S. Zhang, *Macromol. Chem. (Oxford)* **2022**, *55*, 10607; b) X. Li, K. Yang, Z. Li, J. Guo, J. Zheng, S. Li, S. Zhang, T. A. Sherazi, *Int. J. Hydrogen Energy* **2022**, *47*, 15044; c) F. Xu, Y. Chen, X. Cao, J. Li, B. Lin, N. Yuan, J. Ding, *J. Power Sources* **2022**, *545*, 231880.
- [17] J. R. Varcoe, P. Atanassov, D. R. Dekel, A. M. Herring, M. A. Hickner, P. A. Kohl, A. R. Kucernak, W. E. Mustain, K. Nijmeijer, K. Scott, *Energy Environ. Sci.* **2014**, *7*, 3135.
- [18] a) G. Saikia, P. K. Iyer, *J. Org. Chem.* **2010**, *75*, 2714; b) S. Maurya, S. Noh, I. Matanovic, E. J. Park, C. N. Villarrubia, U. Martinez, J. Han, C. Bae, Y. S. Kim, *Energy Environ. Sci.* **2018**, *11*, 3283.
- [19] H. Peng, Q. Li, M. Hu, L. Xiao, J. Lu, L. Zhuang, *J. Power Sources* **2018**, *390*, 165.
- [20] J. Parrondo, Z. Wang, M.-S. J. Jung, V. Ramani, *Phys. Chem. Chem. Phys.* **2016**, *18*, 19705.
- [21] a) Q. H. Zeng, Q. L. Liu, I. Broadwell, A. M. Zhu, Y. Xiong, X. P. Tu, *J. Membr. Sci.* **2010**, *349*, 237; b) S. Wierzbicki, J. C. Douglin, A. Kostuch, D. R. Dekel, K. Kruczała, *J. Phys. Chem. Lett.* **2020**, *11*, 7630.
- [22] a) N. Ye, Y. Xu, D. Zhang, J. Yang, R. He, *Polym. Degrad. Stab.* **2018**, *153*, 298; b) S. Zhang, X. Zhu, C. Jin, *J. Mater. Chem. A* **2019**, *7*, 6883.
- [23] a) X. Peng, T. J. Omasta, E. Magliocca, L. Wang, J. R. Varcoe, W. E. Mustain, *Angew. Chem., Int. Ed.* **2019**, *131*, 1058; b) L. Wang, M. Bellini, H. A. Miller, J. R. Varcoe, *J. Mater. Chem. A* **2018**, *6*, 15404; c) H. Adabi, P. G. Santori, A. Shakouri, X. Peng, K. Yassin, I. G. Rasin, S. Brandon, D. R. Dekel, N. U. Hassan, M.-T. Sougrati, *Mater. Today* **2021**, *12*, 100179; d) W. Ni, H. N. Ul, J. Meibom, Y.-C. Chu, M. Chang, A. Krammer, S. Sun, L. Bai, W. Ma, S. Lee, S. Jin, J. Luterbacher, A. Schueler, H. M. Chen, W. Mustain, X. Hu, *ChemRxiv* **2022**, <https://doi.org/10.26434/chemrxiv-2022-htz7b-v2>; e) N. Zion, J. C. Douglin, D. A.

Cullen, P. Zelenay, D. R. Dekel, L. Elbaz, *Adv. Funct. Mater.* **2021**, *31*, 2100963; f) J. Lilloja, E. Kibena-Põldsepp, A. Sarapuu, J. C. Douglin, M. Käärik, J. Kozlova, P. Paiste, A. Kikas, J. Aruväli, J. Leis, *ACS Catal.* **2021**, *11*, 1920; g) L. Zeng, Y. Liao, J. Wang, Z. Wei, *J. Power Sources* **2021**, *486*, 229377.

- [24] S. Shahgaldi, I. Alaefour, X. Li, *Appl. Energy* **2018**, *225*, 1022.
[25] J.-K. Lee, H. H. Fong, A. A. Zakhidov, G. E. McCluskey, P. G. Taylor, M. Santiago-Berrios, H. D. Abruna, A. B. Holmes, G. G. Malliaras, C. K. Ober, *Macromolecules* **2010**, *43*, 1195.